Effects of slab geometry and obliquity on the interplate thermal regime associated with the subduction of three-dimensionally curved oceanic plates

Ji, Yingfeng

Yoshioka, Shoichi

(Citation)
Geoscience Frontiers,6(1):61-78

(Issue Date)
2015-01

(Resource Type)
journal article

(Version)
Version of Record

(URL)
https://hdl.handle.net/20.500.14094/90005034

Geoscience Frontiers 6 (2015) 61–78

HOSTED BY

Contents lists available at ScienceDirect

China University of Geosciences (Beijing)

Geoscience Frontiers

journal homepage: www.elsevier.com/locate/gsf

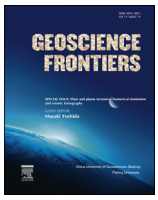

Research paper

Effects of slab geometry and obliquity on the interplate thermal regime associated with the subduction of three-dimensionally curved oceanic plates

Yingfeng Ji [a,*], Shoichi Yoshioka [a,b]

[a] Research Center for Urban Safety and Security, Kobe University, Rokkodai-cho 1-1, Nada Ward, Kobe 657-8501, Japan
[b] Department of Earth and Planetary Science, Graduate School of Science, Kobe University, Rokkodai-cho 1-1, Nada Ward, Kobe 657-8501, Japan

ARTICLE INFO

Article history:
Received 30 August 2013
Received in revised form
15 April 2014
Accepted 21 April 2014
Available online 23 May 2014

Keywords:
Temperature
Mantle flow
Heat flow
Numerical simulation
Slab geometry
Obliquity

ABSTRACT

We investigated the relationships among slab geometry, obliquity, and the thermal regime associated with the subduction of oceanic plates using a three-dimensional (3D) parallelepiped thermal convection model. Various models with convex and concave slab shapes were constructed in the numerical simulation, and the temperature and mantle flow distributions were calculated. The results revealed that when the slab dip angle increases, or the obliquity of subduction becomes steeper, the interplate temperature decreases remarkably. Cooler (warmer) zones on the plate interface were identified from the modeling where there was a larger (smaller) subduction angle. Consequently, the interplate temperature distribution is partly controlled by the true subduction angle (TSA), which is a function of the slab dip angle and the obliquity of subduction. The rate of change of the interface temperature for the TSA was 10–50 °C ($10^\circ < \mathrm{TSA} < 20^\circ$) at depths ranging from $(\mathrm{TSA} - 10) \times 5$ km to $60 + (\mathrm{TSA} - 10) \times 5$ km for a flat slab after a subduction history of 7 Myrs. The along-arc slab curvature affects the variation in TSA. The slab radius also appeared to influence the radius of induced mantle flow.

1. Introduction

The relationship between slab geometry and interplate temperature distribution is an interesting issue. The 3D modeling of oceanic plates has proven to be an effective way to simulate and investigate this relationship. Many 3D numerical simulations of subduction of an oceanic plate in the plate convergent zone have focused on the characteristics of the interplate thermal state (e.g., Chemenda et al., 2000; Morra et al., 2006; Schellart et al., 2007; Yoshioka and Murakami, 2007; Bonnardot et al., 2008; van Keken et al., 2008; Bengtson and van Keken, 2012). However, different slab shapes will produce different temperature distributions and flow patterns associated with the subduction of an oceanic plate. For example, subduction of a curved plate changes the temperature structure beneath the fore-arc zone and significantly affects the thermal regime on a seismically active interface. Studies of seismic tomography (Nakajima and Hasegawa, 2007; Hirose et al., 2008; Zhao et al., 2012) have revealed the geometry of the Pacific and the Philippine Sea (PHS) plates, and provide a possibility for developing subduction models of an oceanic plate with a 3D curved surface (e.g., Toth and Gurnis, 1998; Doin and Henry, 2001; Gurnis et al., 2004; Gerya, 2011) and a presumed fixed trench (Morra et al., 2006, 2010; Stegman et al., 2006; Schellart et al., 2007; Giuseppe et al., 2008). Curved slabs extending beneath overriding plates may significantly affect the plate interface temperature and surface heat flow. Therefore, numerical simulations from subduction models for an arbitrary curved oceanic plate can be used to determine the influence of slab geometry, such as the slab dip angle and obliquity, on the interplate thermal regime. For 3D numerical simulations, numerous researchers have developed fundamental source codes under specified geophysical and geochemical constraints (van Keken and Ballentine, 1991; Gurnis et al., 2004; van Keken et al., 2008). Subduction of an oceanic plate is one of the most challenging and captivating geodynamic processes that can be investigated with numerical techniques (Gerya, 2011). The 3D lateral variability of subduction processes is a new direction in numerical subduction modeling (Honda and Saito, 2003; Honda and Yoshida, 2005; Morra

* Corresponding author. Tel.: +81 80 3831 8062; fax: +81 78 803 5785.
E-mail address: 31911431@qq.com (Y. Ji).

Peer-review under responsibility of China University of Geosciences (Beijing)

http://dx.doi.org/10.1016/j.gsf.2014.04.011

et al., 2006, 2010; Stegman et al., 2006; Honda et al., 2007, 2010; Schellart et al., 2007; Honda, 2009; Zhu et al., 2009, 2011; Jadamec and Billen, 2010; Stadler et al., 2010; Gerya, 2011; Yoshida et al., 2012). Simulation of the subduction of an oceanic plate with a prescribed curved shape is feasible.

However, previous studies of kinematically prescribed inclined slabs have focused on mantle wedge dynamics and small-scale convection (Honda and Saito, 2003; Honda and Yoshida, 2005; Honda et al., 2007, 2010; Zhu et al., 2009, 2011), or the relationship between arc curvature and slab roll-back (Morra et al., 2006, 2010; Stegman et al., 2006; Schellart et al., 2007). Mechanics of slab bending in the mantle associated with subduction has also been studied (Conrad and Hager, 1999; Fukao et al., 2001; Buffett, 2006; Torii and Yoshioka, 2007; Capitanio et al., 2009; Ribe, 2010; Capitanio and Morra, 2012). Some studies have used global or regional high-resolution 3D models of buoyancy-driven slab deformation (Jadamec and Billen, 2010; Stadler et al., 2010). Among them, Tackley (1998, 2000) presented a 3D convection model (stag3D), generating plates through the use of a temperature-dependent viscosity combined with yield stress, although the lateral curvatures on a shallower plate and 3D arbitrary slab shape were not highlighted. Yoshioka and Murakami (2007) proposed that temperature on the plate interface and surface heat flow depended on the shape of the PHS plate that was positioned beneath a continental plate. Although several profiles in the across-arc and along-arc directions have been employed and the interplate thermal regime has been estimated, arbitrary 3D shapes of slabs have not. Consequently, variation in the mantle flow and plate interface temperature in the along-arc direction (*y*-*z* vertical cross-section in Fig. 1b) has not been fully investigated.

In this study, we revised the stag3D code (Tackley and Xie, 2003) to construct a mathematically curved slab model concerning not only the across-arc slab curvature, but also the along-arc curvature, to investigate 3D thermal and mantle flow fields (Fig. 1c). The typical shapes of convex and concave slabs are considered in our numerical simulation. Although the geometries of oceanic plates subducting beneath continental plates are diverse, they are typically convex or concave. The majority of the boundaries of oceanic plates worldwide are concave, although several convex shapes also exist, such as the PHS plate beneath southwest Japan, the Pacific plate beneath northeast Japan, the Juan de Fuca plate beneath Cascadia, and the Nazca plate beneath Columbia and northern Chile. Therefore, we constructed several mathematically expressed 3D slab models with variation in the radius of curvature, and investigated their thermal properties related to slab geometry. The relationships among mantle flow patterns, thermal regime, and slab shape and the operation of the dynamic evolution associated with subduction of an oceanic plate were also determined.

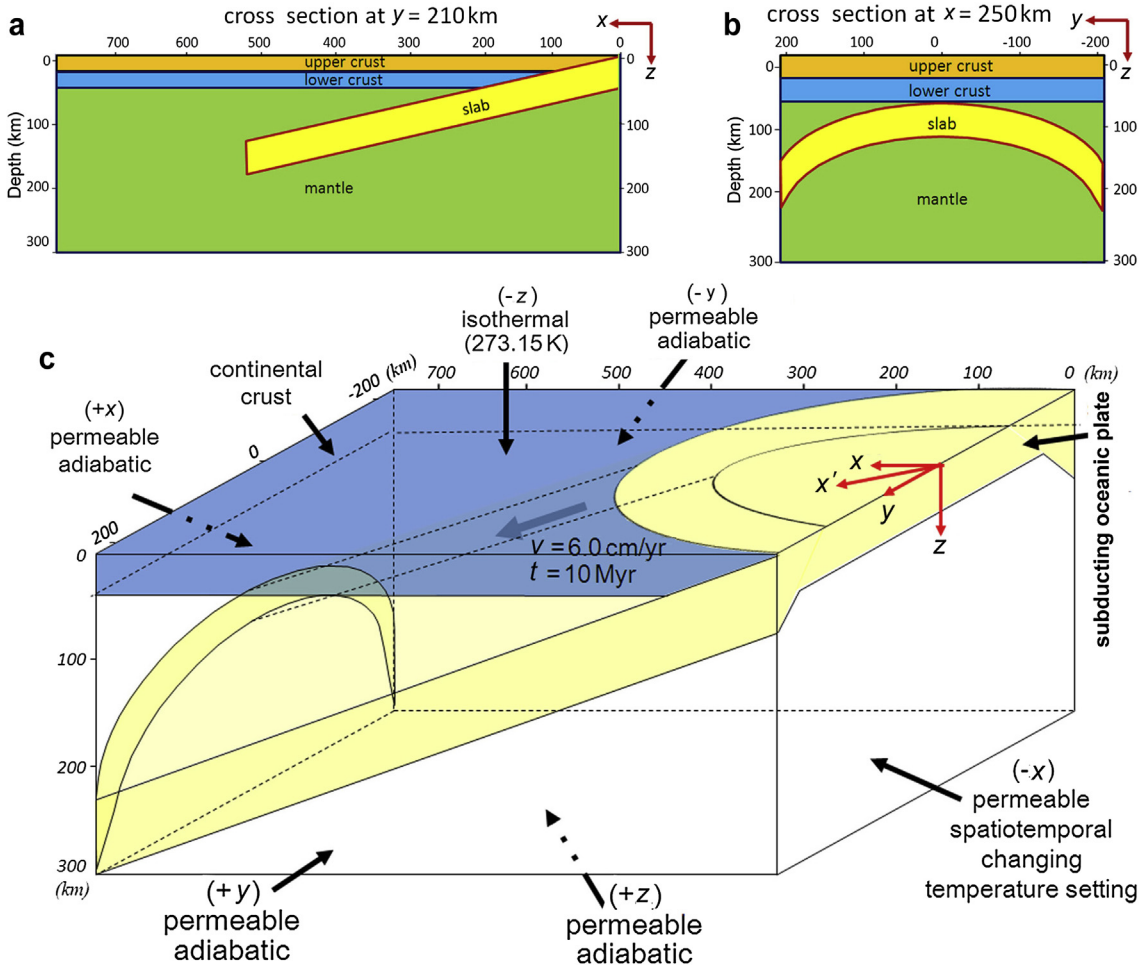

Figure 1. (a) Subdivision of the model domain in the *x*-*z* vertical cross-section at $y = 210$ km. (b) Subdivision of the model domain in the *y*-*z* vertical cross-section at $x = 250$ km. (c) The boundary conditions for Model 3-1. The model is a parallelepiped rectangular box with an isothermal upper surface ($-z$), permeable and adiabatic lower surface ($+z$), permeable and adiabatic left and right sides ($+y$ and $-y$), and permeable and adiabatic front surface ($+x$). The back side ($-x$) is permeable, and a thermal setting is given in Eq. (11).

2. Method and model

Referring to Honda (1997), Yoshioka and Murakami (2007), in the 3D spatiotemporally changing subduction model of an oceanic plate, the equation for the conservation of mass is given by:

$$\nabla\cdot\{\rho_s(z,T)\mathbf{v}\} = 0 \quad (1)$$

where $\rho_s(z,T)$ and $\boldsymbol{v} = (v_1, v_2, v_3)$ are the density as a function of depth z and temperature T, and flow velocity vectors in the Cartesian coordinates, respectively, and the suffix s indicates the adiabatic condition. The momentum equation can be expressed as:

$$-\frac{\partial P}{\partial x_i}+\frac{\partial \tau_{ij}}{\partial x_j}+Ra_0\alpha(T-T_s)\delta_{i3} = 0 \quad (2)$$

where the 3D Cartesian coordinates (x, y, z) are represented by (x_1, x_2, x_3), P is the pressure deviation from hydrostatic pressure, Ra_0 is the Rayleigh number, α is thermal expansivity, T is temperature, τ_{ij} is a stress tensor, and δ_{ij} is the Kronecker delta. T_s can be written as:

$$\frac{dT_s}{dx_3} = Di_z T_s \quad (3)$$

The dissipation number Di_z is given as:

$$Di_z = \frac{g\alpha D}{C_p} \quad (4)$$

where g is gravitational acceleration, D is the thickness of the model, and C_p is the specific heat at constant pressure. The Rayleigh number at the model surface Ra_0 is given by:

$$Ra_0 = \frac{g\alpha_0 D^3\Delta T}{\eta_0\kappa_0} \quad (5)$$

where ΔT is the difference in temperature between the top and bottom model boundaries, and η_0 and κ_0 are dynamic viscosity and thermal diffusivity at the model surface, respectively. The density ρ depends on temperature:

$$\rho = \rho_s(z,T)\{1-\alpha(T-T_s)\} \quad (6)$$

The energy equation is expressed as:

$$\rho C_p\left(\frac{\partial T}{\partial t}+\mathbf{v}\cdot\nabla T\right) = k\nabla^2 T+\eta(\nabla v)^2+\rho g\alpha T v+\rho H \quad (7)$$

where the left side of the equation is the variation in energy in a unit volume, including the advection term $\rho C_p\mathbf{v}\cdot\nabla T$. On the right side, a heat diffusion term, $k\nabla^2 T$, viscous dissipation term, $\eta\,(\nabla v)^2$, adiabatic compression term, $\rho g\alpha T v$, and radioactive heating term, ρH, are included. H is the internal heating per unit mass.

For viscosity η, the following form of Christensen (1996) was used:

$$\eta = \eta_0\exp\left\{\frac{T_0-T}{a}+\frac{z}{b}-\left(\frac{z}{c}\right)^2\right\} \quad (8)$$

where a, b, and c are the coefficients. The values of the model parameters used in this study are given in Table 1. The initial temperature condition for the parallelepiped box model is given by:

$$T = T_0 erf\left(\frac{z}{2\sqrt{\frac{k_0 t_{cont}}{\rho_0 Cp_0}}}\right) \quad (9)$$

with

$$t_{cont} = \left(\frac{d_{cont}}{I}\right)^2 \quad (10)$$

Where t_{cont} and d_{cont} are age (Myr) and thickness (km) of the continental crust, respectively. In this study, d_{cont} and t_{cont} were assumed to be 32 km and 18.2 Myr, respectively. I is the thickness/age relation, given as 7.5 km/(Myr)$^{1/2}$, following Yoshii (1975).

The initial temperature condition at trench side ($-x$ face in Fig. 1c) is:

$$T = T_0 erf\left(\frac{z}{2\sqrt{\frac{k_0 t_{ocea}}{\rho_0 Cp_0}}}\right) \quad (11)$$

with

$$t_{ocea} = \left(\frac{d_{ocea}}{I}\right)^2 \quad (12)$$

where t_{ocea} and d_{ocea} are age (Myr) and thickness (km) of the oceanic plate, respectively. d_{ocea} and t_{ocea} were assumed to be 30 km and 16 Myr, respectively.

Eqs. (1), (2) and (7) are solved at each time step using a finite difference and finite volume method, and the temperature and flow velocity are obtained. The number of grids used in this study was $72\times72\times72$, which were equally spaced with regular intervals of 10.7 km in length, 11.7 km in width, and 4.2 km in depth (Fig. 1c). The time step was 0.025 Myrs.

When we consider the curvature of the slab in the y-z vertical cross-section being parallel to the trench axis, it mathematically becomes a half annulus (Fig. 1b). We idealized it into a simple model with the curvature being proportional to the distance from the trench. Thus, we chose a half elliptic cylinder surface to represent the upper surface of the slab (Model 3, Fig. 2c). Its curvature can also be a function of the distance from the trench. We also considered another slab shape, which was similar to a tapering half elliptic cylindrical surface and is hereafter referred to as a conic surface (Model 2, Fig. 2b), with a radius of curvature proportional to the distance towards the trench. Therefore, the curvature of the slab surface gradually changed from a flat to an ellipsoid surface, from the trench to the other end. This model contrasted well with the half elliptic cylindrical slab model with a constant surface curvature (Fig. 2c). For comparison, we also constructed a model with a flat slab surface with a curvature of zero (Model 1, Fig. 2a), and an

Table 1
The values of model parameters for numerical simulations of subduction of three-dimensional curved slabs.

Symbol	Parameters	Value	Units
ρ_0	Standard density	$3.3\times10^{3(1)}$	kg/m^3
T_0	Standard temperature	1.6×10^{3}	K
k_0	Standard thermal conductivity	$2.9^{(3)}$	W/(m·K)
Hr	Radioactive heat generation rate in the mantle	$2.245\times10^{-13(1)}$	W/m^3
C_{p_0}	Standard specific heat at constant pressure	$1.2\times10^{3(1)}$	J/(kg·K)
κ_0	Thermal diffusivity at the model surface	$7.6\times10^{-7(4)}$	m^2/s
η_0	Standard viscosity	$1.0\times10^{20(3)}$	Pa·s
α_0	Standard thermal expansion	$3.0\times10^{-5(2)}$	K^{-1}
v_0	Subduction velocity	6.0	cm/yr
a	Constant coefficient in Christensen's formula	$131.3^{(3)}$	
b	Constant coefficient in Christensen's formula	$2.36\times10^{5(3)}$	
c	Constant coefficient in Christensen's formula	$1.086\times10^{6(3)}$	

Note: [1] Wang et al., 1995; [2] Iwamori, 1997; [3] Christensen, 1996; [4] Yoshioka and Murakami, 2007.

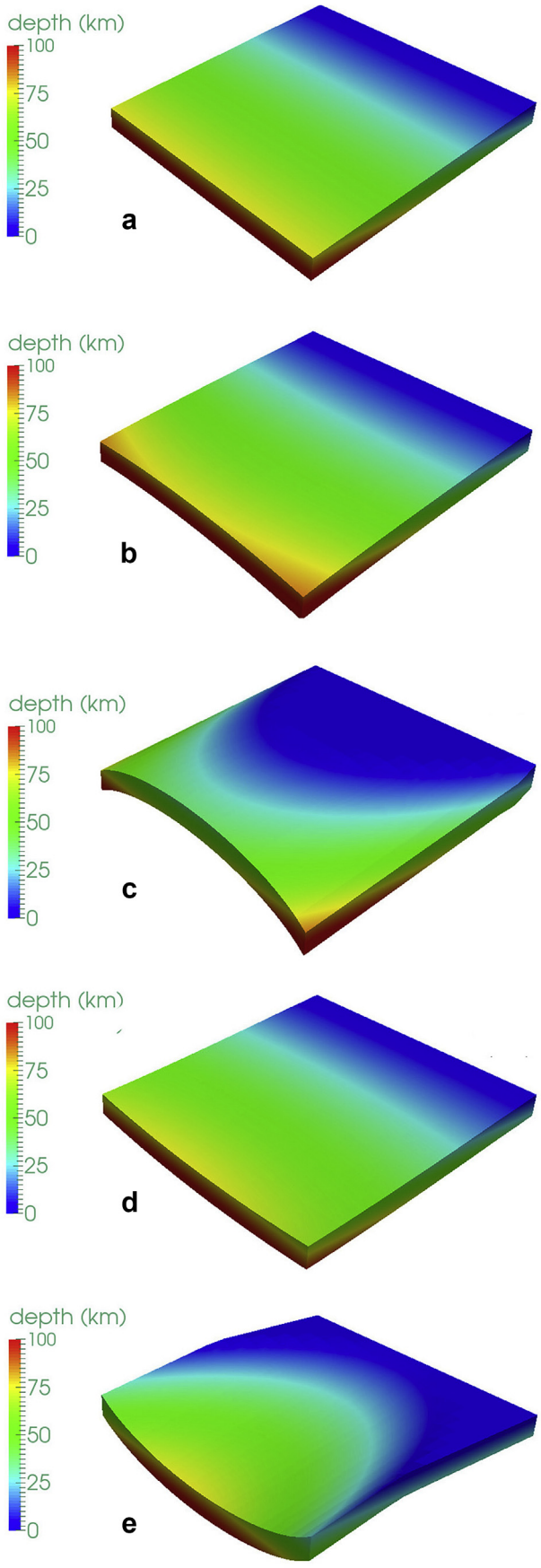

inverse conic surface (Model 4, Fig. 2d), with the shape of a conic slab as used in Model 2 that was then turned upside-down, and an inverse half elliptic cylinder surface (Model 5, Fig. 2e) that was a turned-over version of Model 3. For Models 4 and 5, the curvature had a negative value. In cylindrical Model 3 (Fig. 2c) and inverse cylindrical Model 5 (Fig. 2e), the trench axes were curved with ellipse lines.

Hence, we constructed five basic types of slab shape (Fig. 2): (1) simple flat surface (Model 1), (2) conic surface (Model 2), (3) cylindrical surface (Model 3), (4) inverse conic surface (Model 4), and (5) inverse cylindrical surface (Model 5). In addition, two kinds of plate motion were considered: normal to the trench axis and oblique subduction. It was important to determine how the slab shape interacts with oblique subduction. We subdivided the five models into 10 categories with straight and oblique subduction taken into account. We used the suffix 1 to represent straight subduction, and the suffix 2 for oblique subduction, thus the slab Models i-j ($i = 1$ to 5; $j = 1, 2$) are the 10 categories we consider here. We used i to represent the models described above. Model i-1 and Model i-2 denote models for straight subduction and oblique subduction, respectively.

The five models with differently shaped slabs were set in a parallelepiped box with a length of 771 km, a width of 420 km, and a depth of 300 km (Fig. 1c). Subduction of an oceanic plate began from the top-right and finished in the bottom-left, crossing a horizontal distance of 771 km. Because the ocean floor can be represented as being flat, we set the surface of the oceanic plate to be flat at the top of Models 3-j and 5-j ($j = 1, 2$), where the oceanic plate began to subduct along the curved trench.

To assign a prescribed velocity only for the subducting oceanic plate, we differentiated the part of the slab with a thickness of 30 km using a prescribed guide. As can be seen in the cross-sections in Fig. 1a and b, the slab section for Model 3 was designed as a half elliptical ring.

The boundary conditions for the models were an isothermal upper surface ($-z$), permeable, adiabatic bottom ($+z$), left side ($+y$), right side ($-y$), front surface ($+x$), and permeable back side ($-x$) with an initial thermal setting as designated in Eq. (11). The initial temperature condition for the model is given by Eq. (9). The subduction velocity inside the slab was prescribed by Eqs. (A6–A8). The temperature and mantle flow in the model were calculated at each time step. Based on these settings, numerical simulations for 10 curved slab models were performed.

3. Results

3.1. Thermal regime, true subduction angle (TSA), and the rate of temperature change for TSA

The relationship among obliquity, dip angle, and the true subduction angle (TSA) was investigated. According to the curvature of space curves, the rate of variation in an angle at a point on a curve is defined as the reciprocal of the length of the radius of curvature, also referred to as the curve's space curvature at the point in question. Here, we defined the concept of TSA as the subduction angle of an oceanic plate along its oblique subducting direction. If it is subducting in a straight line, the

Figure 2. Bird's eye view of the slab models constructed in this study. Subduction of the oceanic plate takes place leftward and downwards from the trench (right top). The color denotes the depth of the surface of the slab (km). (a) Flat slab (Model 1, including straight subduction referred to as Model 1-1 and oblique subduction as Model 1-2). (b) Conic shape slab (Model 2, including Models 2-1 and 2-2). (c) Cylindrical shape slab (Model 3, including Models 3-1 and 3-2). (d) Inverse conic slab (Model 4, including Models 4-1 and 4-2). (e) Inverse cylindrical slab (Model 5, including Models 5-1 and 5-2).

TSA is the same as the dip angle of the oceanic plate. However, for an oblique subduction, the TSA does not equal the dip angle. It also depends on the obliquity azimuth and curvature of the slab.

As shown in Fig. 3, we assumed that a point S on the slab surface subducts from point O to point A landward obliquely. At point O, the horizontal obliquity azimuth of the slab was assumed to be $\alpha(O)$. Then, the across-arc dip angle is $\theta_l(O)$ and the along-arc dip angle is $\theta_t(O)$. The TSA at point O is represented by $TSA(O)$, which is the angle between the subduction vector and the ground surface. When point S moves to point A, $TSA(O)$, $\theta_l(O)$, and $\theta_t(O)$ become $TSA(A)$, $\theta_l(A)$, and $\theta_t(A)$, respectively. The total length of curve OA is $\overline{OA}$. We noticed that the variation in the dip angles $\Delta\theta_l$ and $\Delta\theta_t$ were dependent on the integral of slab curvature via the subducting path OA. If one part of the length of the subducting pathway OS is s, then the subduction obliquity is $\alpha(s)$. The slab curvature along the velocity direction at point S is $C_v(s)$, and the rate of change in TSA is $TSA'(s) = C_v(s)$. Here, $C_v(s)$ includes both the across-arc and along-arc curvatures of the slab. The across-arc curvature at point S is also the rate of change in θ_l, i.e., $\theta_l'(s) = \frac{C_v(s)}{\cos\alpha(s)}$, and the along-arc curvature at point S is $\theta_t'(s) = \frac{C_v(s)}{\sin\alpha(s)}$. Then we have:

$$\Delta\theta_l = \theta_l(A) - \theta_l(O) = \int_0^{\overline{OA}} \frac{C_v(s)}{\cos\alpha(s)} ds \tag{13}$$

$$\Delta\theta_t = \theta_t(A) - \theta_t(O) = \int_0^{\overline{OA}} \frac{C_v(s)}{\sin\alpha(s)} ds \tag{14}$$

$$\Delta\alpha = \alpha(A) - \alpha(O) = \int_0^{\overline{OA}} \alpha'(s) ds \tag{15}$$

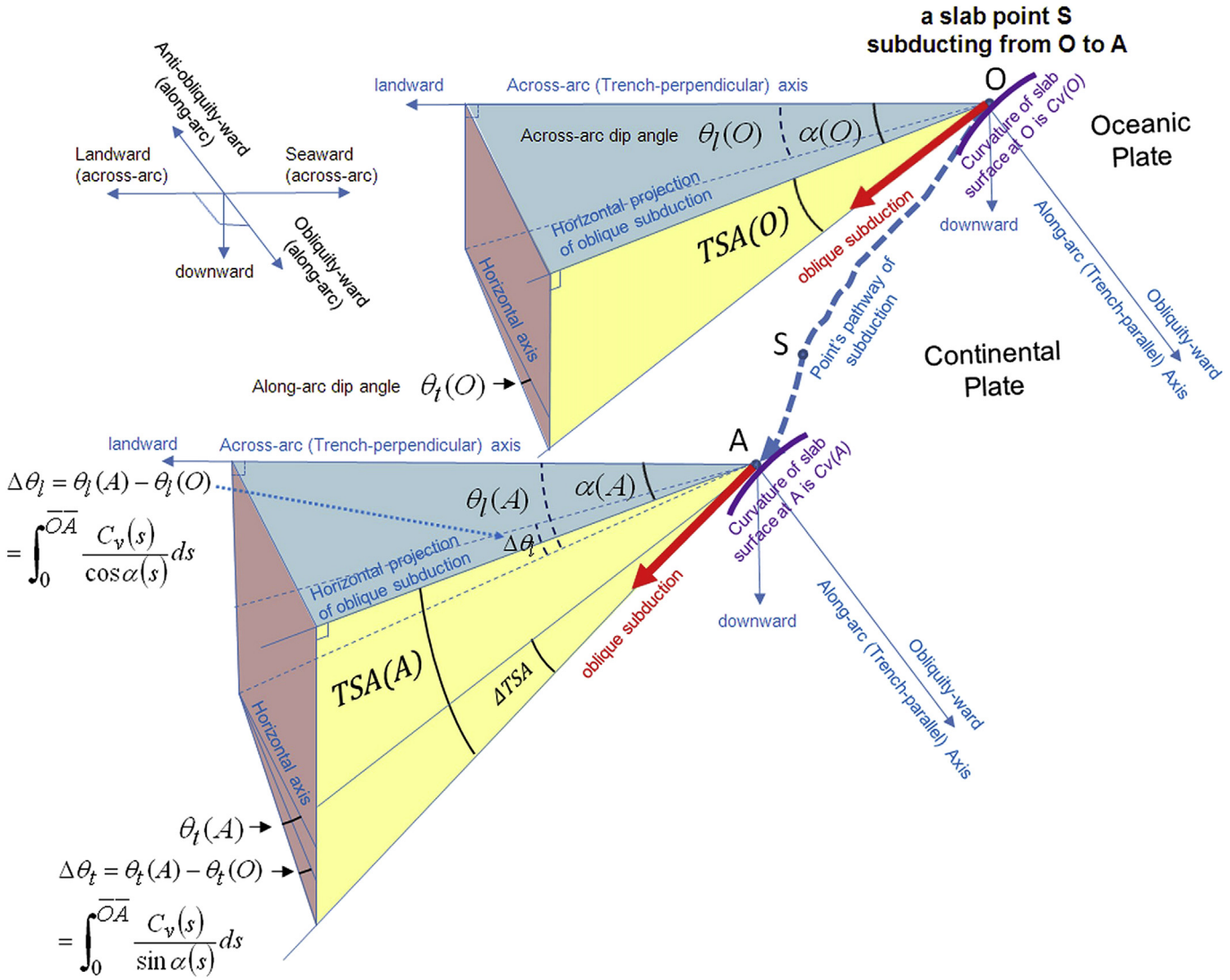

Figure 3. Schematic figure of the definition of the true subduction angle (TSA). O and A are arbitrary points on the slab surface. Point S on the slab is obliquely subducted from point O to point A. The obliquity is α. The across-arc dip angle is θ_l and the along-arc dip angle is θ_t. The TSA is the angle between the subduction vector and the horizontal surface. The rate of change in TSA depends on the slab curvature C_v, and the calculation of TSA is given by Eqs. (16) and (17).

Using the infinitesimal geometry and trigonometric function, the TSA at point A can be defined as follows:

$$TSA(A) = \arctan[\cos\alpha(A)\cdot\tan\theta_l(A) + \sin\alpha(A)\cdot\tan\theta_t(A)] = f[\alpha(A),\theta_l(A),\theta_t(A)] \quad (16)$$

or:

$$TSA(A) = \arctan\left[\cos\left\{\alpha(O)+\int_0^{\overline{OA}}\alpha'(s)ds\right\}\cdot\tan\left\{\theta_l(O)+\int_0^{\overline{OA}}\frac{C_v(s)}{\cos\alpha(s)}ds\right\}+\sin\left\{\alpha(O)+\int_0^{\overline{OA}}\alpha'(s)ds\right\}\cdot\tan\left\{\theta_t(O)+\int_0^{\overline{OA}}\frac{C_v(s)}{\sin\alpha(s)}ds\right\}\right] = f[\alpha(O),\theta_l(O),\theta_t(O),\alpha'(s),C_v(s)] \quad (17)$$

If obliquity does not change during the subduction, Eq. (17) can be simplified as:

$$TSA(A)=\arctan\left[\cos\alpha(O)\cdot\tan\left\{\theta_l(O)+\int_0^{\overline{OA}}\frac{C_v(s)}{\cos\alpha}ds\right\}+\sin\alpha(O)\cdot\tan\left\{\theta_t(O)+\int_0^{\overline{OA}}\frac{C_v(s)}{\sin\alpha}ds\right\}\right] =f[\alpha(O),\theta_l(O),\theta_t(O),C_v(s)] \quad (18)$$

Eqs. (16–18) indicate that $TSA(A)$ is an arctangent function of the composite of the obliquity azimuth α, the dip angles θ_l and θ_t, and slab curvatures $C_v(s)$. Eq. (16) can be used to make a direct estimate of the value of TSA at a point where the instant values of α, θ_l, and θ_t are known. Eqs. (17) and (18) were used to determine the relationship between the TSA and 3D curvature of the slab along the subduction direction. If we know the curvature of the slab along the pathway OA in the direction of subduction, Eqs. (17) and (18) can also be used to calculate the value of $TSA(A)$ by $\alpha(O)$, $\theta_l(O)$, $\theta_t(O)$, and $C_v(s)$.

Eqs. (16–18) also explain why the TSA is similar to the dip angle and obliquity azimuth. It is actually a combination of obliquity and the dip angle of a slab. Because a cold slab is heated by the hot surrounding upper mantle, the duration of heating is critical to determine the slab-mantle interface temperature. A smaller TSA corresponds to a longer stay in the mantle, and results in a hotter slab. Therefore, for slabs at the same depth, a larger overall TSA indicates a shorter heating time, resulting in a low-temperature zone at the plate interface.

If we assume $\alpha = 0$, which indicates a straight subduction, then:

$$TSA(A) = \theta_l(O) + \int_0^{\overline{OA}}\frac{C_v(s)}{\cos\alpha(s)}ds = \theta_l(A) \quad (19)$$

that is, the TSA is equal to the dip angle in a straight subduction.

For a flat slab, because $C_v(s)$ equals zero, and α, θ_l, and θ_t are invariant, Eq. (13) can be simplified as:

$$TSA = \arctan(\cos\alpha\cdot\tan\theta_l + \sin\alpha\cdot\tan\theta_t) = f(\alpha,\theta_l,\theta_t) \quad (20)$$

Furthermore, for a flat slab without transverse (along-arc) tilt, i.e., $\theta_t(O) = 0$, Eq. (20) can be simplified further to:

$$TSA = \arctan(\cos\alpha\cdot\tan\theta_l) \quad (21)$$

which was applied in Model 1.

Eq. (21) can also be used to make a rough estimate of the TSA if the value of α is comparatively small and θ_t is unknown.

To further investigate how the TSA influences the thermal regime, we undertook a quantitative comparison of the dip angle θ_l, α, TSA, and interplate temperature distribution $T(d)$; here d is the distance along the profile from the trench. For the dip angle, θ_l equals to 10° in Fig. 4a and θ_l equals to 20° in Fig. 4b. The curves 2 to 10 are the temperature profiles for $TSA = 2°–10°$ with a decrease of 1° for each curve. The depth of the interface is shown by the pink line. The slope of the pink line can also be considered the dip angle. Hence, a comparison of temperatures at the same depth can be made. We found that the temperature increased and gradually flattened as the interface goes deeper and farther from the trench. However, the interface temperature differs according to the different TSA and obliquity, as marked in Fig. 4. Even at the same dip angle, the different obliquity and TSA resulted in a different temperature curve but was enveloped within a leaf-like zone, which was constrained by the uppermost envelope curve of temperature without slab subduction, and the lowest envelope curve of temperature with a straight subduction. The nine curves were more equidistant than those obtained for obliquity, indicating that the TSA rather than the obliquity has a more linear corresponding relationship with the interface temperature.

When the dip angle was 10° (Fig. 4a), the plate interface temperature was raised by ~120 °C due to the decrease in TSA from 10° to 2°. When the TSA dropped from 10° to 9°, the increase in the interplate temperature was 50–70 °C at a depth of 30–60 km. When the TSA dropped from 7° to 6°, the increase in the temperature was 50–80 °C at a depth of 20–30 km. The depth of interface temperature that was sensitive to a changing TSA became shallower when the TSA was gradually reduced. Overall, we found that for every decrease of 1° in the TSA, the plate interface temperature dropped by a maximum of almost 50 °C at depths within the range of 10–60 km. For example, at continental Moho (almost 30 km depth), when the TSA changed from 10° to 5°, the plate interface temperature would rise by 300–350 °C (blue line AA′ in Fig. 4a), which was considered to be most of the zone in which the TSA was most sensitive to the interplate temperature in this study. Coincidentally, it is also known to be a contact zone for oceanic and continental crusts, and is seismically active.

We also compared the interface temperature profile with a dip angle of 20° (see Fig. 4b). The temperature drop was nearly 15 °C for every decrease of 1° in the TSA within the depth range of 60–110 km. We also found that this range of depths increased with an increase in the dip angle. It is possible that this depth is a sine function of the dip angle. For example, in Fig. 4a and b, the depths are approximated to the product of the sine function of dip angle and the length of the slab, over the depth range of 200–300 km. The graphs show that if the depth becomes deeper than 150 km, the variation in the TSA will have a much weaker effect on the interface temperature.

From a comparison of the temperature curves, we concluded that the rate of change in interface temperature for the TSA was about 10–50 °C/° within the sensitive depth domain for a changing TSA. This was approximated to be $[(TSA - 10)\times5$ km, $60 + (TSA - 10)\times5$ km] $(10° < TSA < 20°)$ for a flat slab with a subduction history of 7 Myrs.

However, the crustal heat flow had a very different relationship with the TSA (Fig. 5). Although the parameters used were the same as those shown in Fig. 4, the change in surface heat flow in the scenario shown in Fig. 5a was approximately 15 mW/m^2 as the TSA changed from 4° to 3° when the depth of the plate interface was

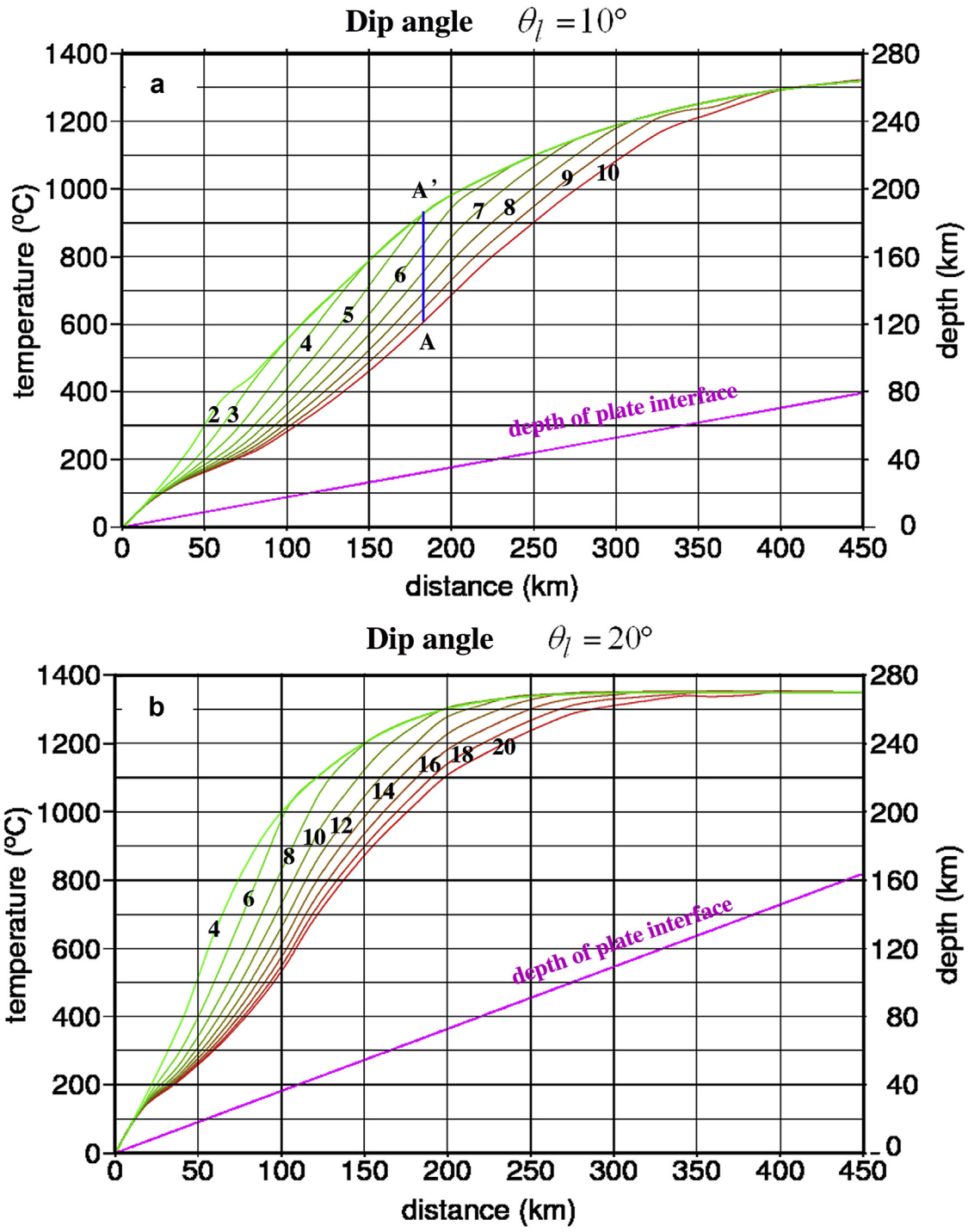

Figure 4. The calculated interplate thermal regime along profiles in the trench-perpendicular direction with various obliquities (counter-clockwise from the straight subduction) and different dip angles at 7 Myr. The pink line indicates the variation in the depths of the plate interface along the profiles. (a) The interplate temperature distribution when the dip angle is equal to 10°. Curve 10: TSA = 10°, Obliquity = 0°; Curve 9: TSA = 9°, Obliquity = 26.1°; Curve 8: TSA = 8°, Obliquity = 37.2°; Curve 7: TSA = 7°, Obliquity = 45.9°; Curve 6: TSA = 6°, Obliquity = 53.4°; Curve 5: TSA = 5°, Obliquity = 60.3°; Curve 4: TSA = 4°, Obliquity = 66.6°; Curve 3: TSA = 3°, Obliquity = 72.7°; Curve 2: TSA = 2°, Obliquity = 78.6°. (b) The interplate temperature distribution when the dip angle is equal to 20°. Curve 20: TSA = 20°, Obliquity = 0°; Curve 18: TSA = 18°, Obliquity = 26.8°; Curve 16: TSA = 16°, Obliquity = 38.0°; Curve 14: TSA = 14°, Obliquity = 46.8°; Curve 12: TSA = 12°, Obliquity = 54.3°; Curve 10: TSA = 10°, Obliquity = 61.0°; Curve 8: TSA = 8°, Obliquity = 67.3°; Curve 6: TSA = 6°, Obliquity = 73.2°; Curve 4: TSA = 4°, Obliquity = 78.9°.

10 km. The uppermost envelope for the group of curves should be a temperature curve with an infinitesimal TSA. The rate of change in heat flow with an increase in TSA was slower, and reached a maximum of 3 mW/(m^2 °) for a dip angle of 10° (Fig. 5a) when the depth of the plate interface was within the range of 0 to 40 km, and was a maximum of 2 mW/(m^2 °) for a dip angle of 20° (Fig. 5b) when the depth of the plate interface was within a range from 0 to 50 km. This is because the crustal heat flow is determined not only by the interplate temperature, but also by the depth from the surface. When the plate interface was deeper than 40 to 60 km, the effects of interplate temperature and the TSA were barely apparent. Thus, the effect of the TSA on crustal heat flow was comparatively

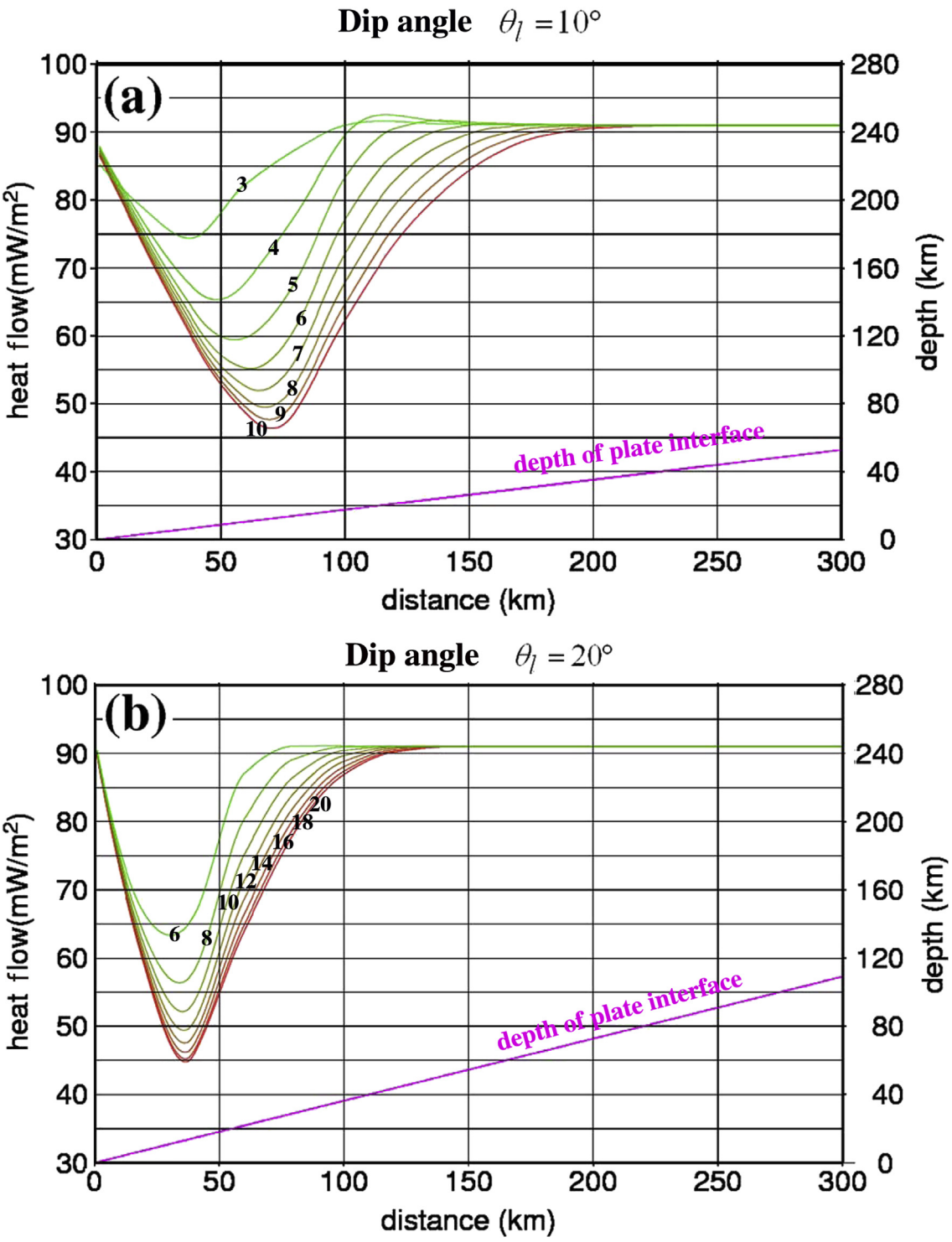

Figure 5. The surface heat flow distribution calculated along profiles in the trench-perpendicular direction with various obliquities (counter-clockwise from the straight subduction) and different dip angles at 7 Myr. The pink line indicates the variation in the depth of the plate interface along the profiles. (a) Surface heat flow distribution when the dip angle is equal to 10°. The curves have the same TSA and obliquity as those shown in Fig. 4a. (b) Surface heat flow distribution when the dip angle is equal to 20°. The curves have the same TSA and obliquity as shown in Fig. 4b.

low when TSA >10°. The rate of change in surface heat flow for the TSA with a dip angle of 10° was ~15 mW/(m^2 °) (0° < TSA < 5°), and ~3 mW/(m^2 °) (5° < TSA < 10°). For a dip angle of 20°, the rate of change was ~15 mW/(m^2 °) (0° < TSA < 5°), ~3 mW/(m^2 °) (5° < TSA < 10°), and ~2 mW/(m^2 °) (10° < TSA < 20°). The sensitive depth of the plate interface for the TSA was 0–50 km for a flat slab with a subduction for 7 Myrs.

The quantitative calculation of the thermal regime described above was performed using Model 1 with a flat slab. A qualitative comparison of the various curved slabs was undertaken based

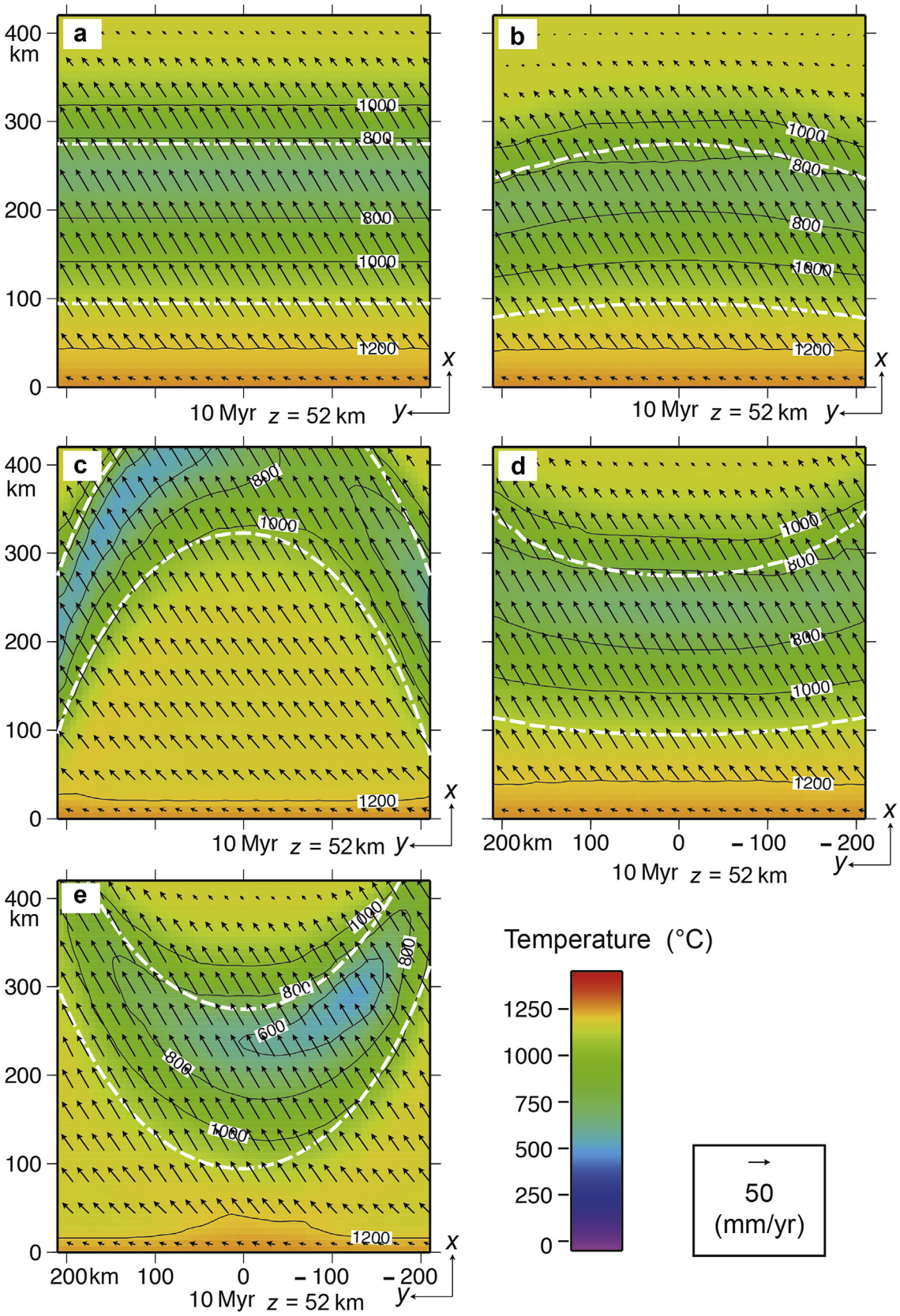

Figure 6. The temperature and mantle flow distributions calculated at a depth of 52 km in the models with five different slab shapes at 10 Myr. The oceanic plate at the bottom subducts at 6.0 cm/yr in an upward direction. Oblique subduction at 30° counter-clockwise from the normal direction of the trench occurs and the dip angle at the trench is 10°. The two white dotted lines indicate the upper and lower surfaces of the subducting oceanic plate. (a) Flat slab with oblique subduction (Model 1-2). (b) Conic slab with oblique subduction (Model 2-2). (c) Cylindrical slab with oblique subduction (Model 3-2). (d) Inverse conic slab with oblique subduction (Model 4-2). (e) Inverse cylindrical slab with oblique subduction (Model 5-2).

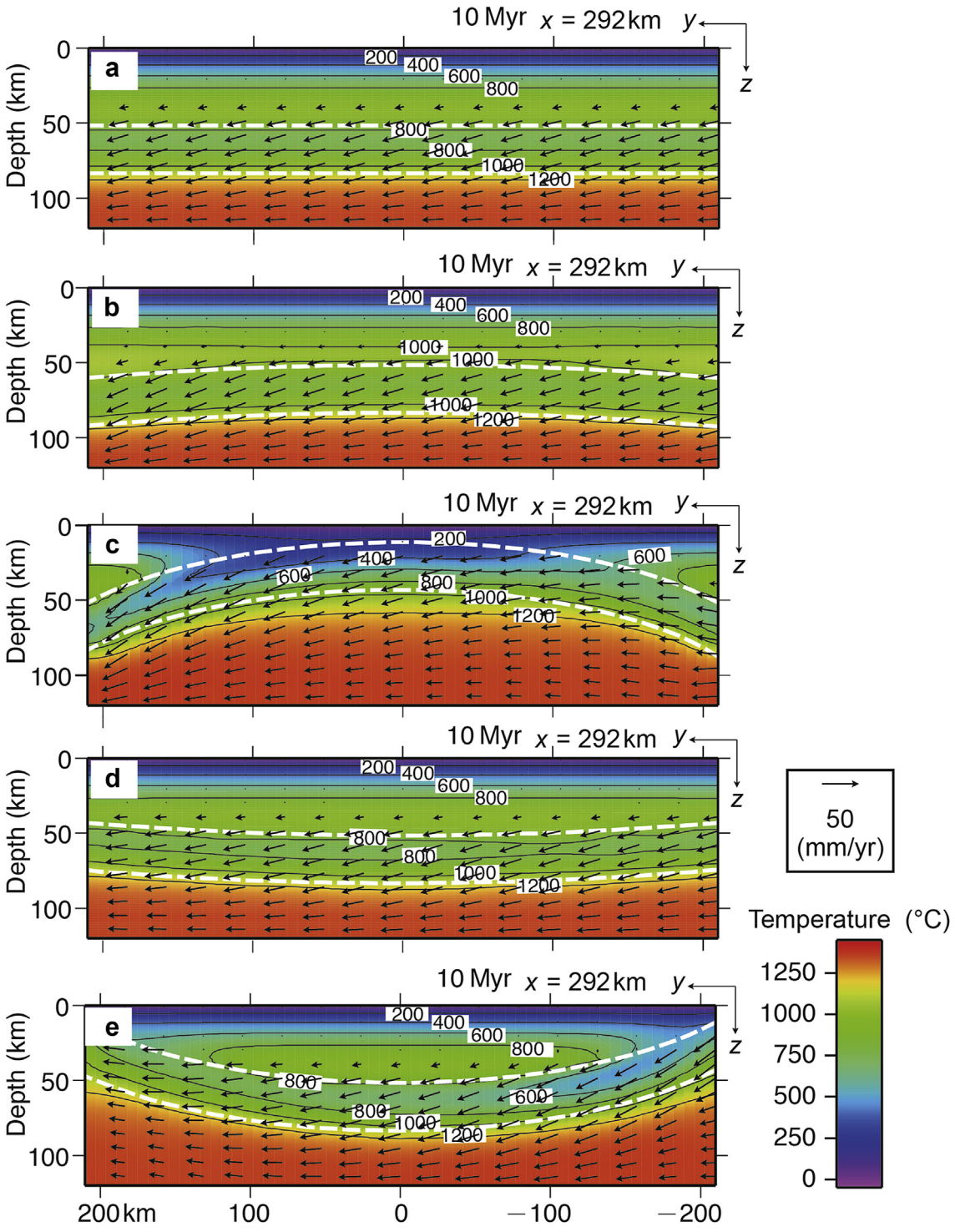

Figure 7. The temperature and mantle flow distributions calculated in the y-z vertical cross-section at $x = 292$ km in the models with the five different shapes of the slabs at 10 Myr. The oceanic plate subducts at 6.0 cm/yr. Oblique subduction at 30° counter-clockwise from the normal direction of the trench occurs and the dip angle at the trench is 10°. The two white dotted lines indicate the upper and lower surfaces of the subducting oceanic plate. (a) Flat slab (Model 1-2). (b) Conic slab (Model 2-2). (c) Cylindrical slab (Model 3-2). (d) Inverse conic slab (Model 4-2). (e) Inverse cylindrical slab (Model 5-2).

on all of the curved slab models in the following sections (3.2 to 3.4).

3.2. Comparison of temperature and flow velocity

Figs. 6–8 show the spatial distributions of temperature and mantle flow at 10 Myr. Fig. 6 shows the *x*-*y* horizontal cross-section at a depth of 52 km, and Fig. 7 shows the *y*-*z* vertical cross-section at a distance of 292 km from the trench. Fig. 8 shows the *x*-*z* vertical cross-section at two profiles $y = -140$ km and $y = 0$ km for straight subduction. By comparing these figures, the following results were obtained.

First, different patterns of temperature and mantle flow were revealed. The spatiotemporal variation in mantle flow differs

remarkably due to the different shapes of the slab surfaces. The shape of the slabs generated different patterns of temperature distribution at the same depth in the mantle (Fig. 6). For the flat slab, the isothermal contour lines were almost parallel and gradually changed with distance from the trench (Fig. 6a). In the case of a conic slab, the isothermal contour lines were slightly curved where the conic slab just began to curve (Fig. 6b and d), and cylindrical shapes appeared (Fig. 6c and e). Therefore, we concluded that the temperature distribution at the same depth had a close relationship with the shape of the slab. Their isothermal contour lines were curved like the slab surface geometry. This also implies that the mantle temperature distribution just above the slab had a closely corresponding relationship with the shape of the slab surface at a certain depth.

Second, the mantle flow pattern fluctuates more remarkably with the increasing curvature of the slab (Fig. 6b to c, or d to e). Driven by the subduction of the oceanic plate, mantle substances moved together with a smaller velocity than inside the slab (left side in Fig. 6, lower half in Fig. 7). For oblique subduction, the slab yielded convection in the mantle from the transverse (y) direction in Model 3 (Fig. 7c) more remarkably than in Models 2 and 4 (Fig. 7b and d).

Interestingly, the flow velocity of the slab moving upward along the slab slope (right side in Fig. 7c) had more of an upward trend than the slab moving down the slab slope (left side in Fig. 7c). It seems that the subduction angle is changed by the slab slope, although in reality the figure shows the projection of the TSA on the cross-section. This indicates the asymmetry of the flow field for the oblique subduction of a symmetric slab where the TSA differs. The

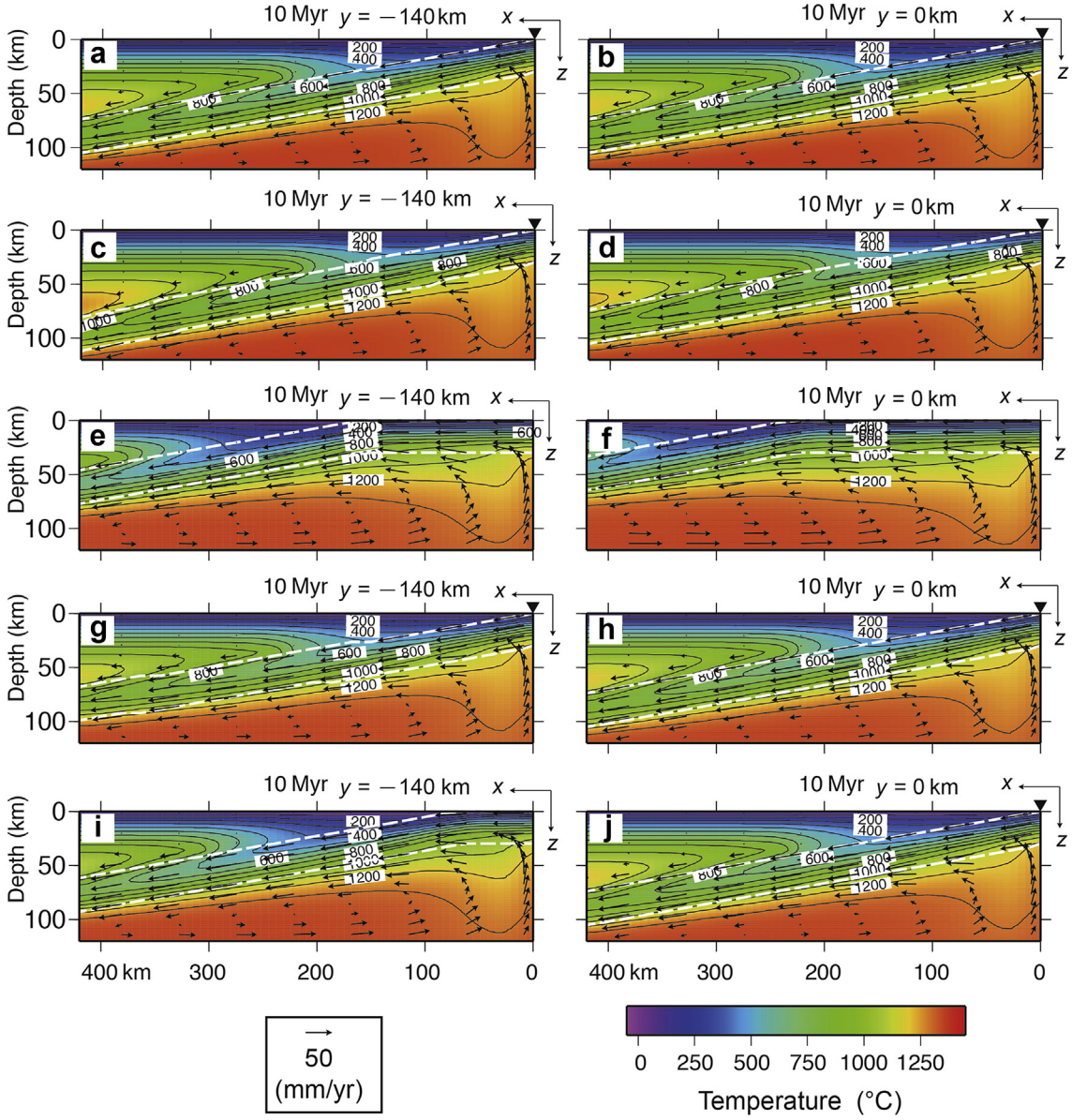

Figure 8. The temperature and mantle flow distributions calculated in the x-z vertical cross-section at $y = -140$ km and $y = 0$ km with the five different shapes of the slabs at 10 Myr. The oceanic plate subducts at 6.0 cm/yr leftward with a dip angle of 10°. The two white dotted lines indicate the upper and lower surfaces of the subducting oceanic plate. The inverse solid triangle indicates the location of the trench. (a) Flat slab with straight subduction (Model 1-1) at $y = -140$ km. (b) Flat slab with straight subduction (Model 1-1) at $y = 0$ km. (c) Conic slab with straight subduction (Model 2-1) at $y = -140$ km. (d) Conic slab with straight subduction (Model 2-1) at $y = 0$ km. (e) Cylindrical slab with straight subduction (Model 3-1) at $y = -140$ km. (f) Cylindrical slab with straight subduction (Model 3-1) at $y = 0$ km. (g) Inverse conic slab with straight subduction (Model 4-1) at $y = -140$ km. (h) Inverse conic slab with straight subduction (Model 4-1) at $y = 0$ km. (i) Inverse cylindrical slab with straight subduction (Model 5-1) at $y = -140$ km. (j) Inverse cylindrical slab with straight subduction (Model 5-1) at $y = 0$ km.

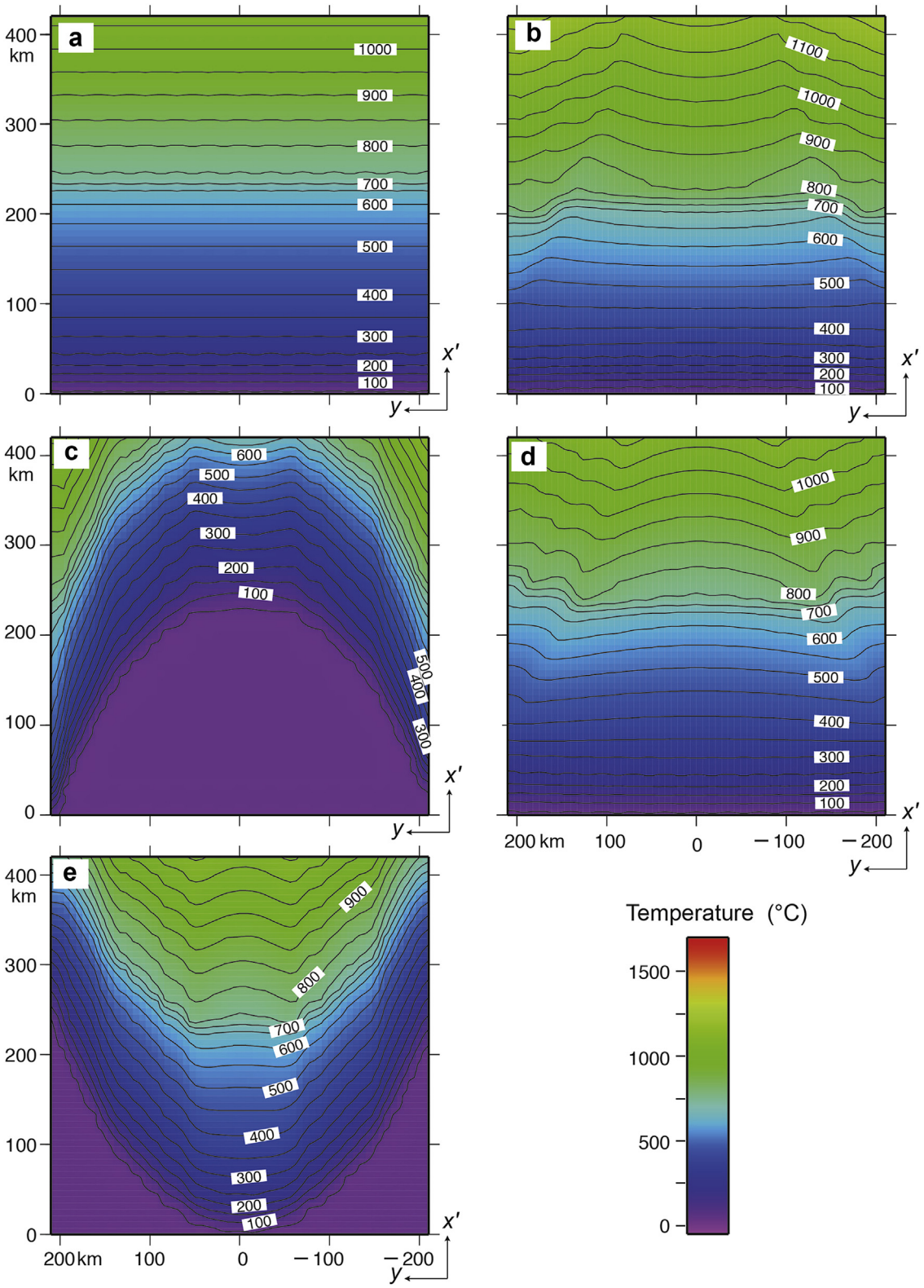

Figure 9. The interplate temperature distribution calculated for the five different slab shapes at 10 Myr. The oceanic plate subducts at 6.0 cm/yr in the x' direction with a dip angle of 10°. x' is taken along the dipping direction, as shown in Fig. 1c. (a) Flat slab (Model 1-1). (b) Conic slab (Model 2-1). (c) Cylindrical slab (Model 3-1). (d) Inverse conic slab (Model 4-1). (e) Inverse cylindrical slab (Model 5-1).

TSA is the slope angle in the subduction direction at that point. Therefore, the oblique subduction of a curved oceanic plate would cause differences in the direction of velocity at different positions on a curved slab.

Third, the isothermal contour lines revealed that the portion where the oceanic plate subducts more steeply tended to have a lower temperature distribution within the slab, as shown on the left side of Fig. 6c and right side of Fig. 6e. Although the curvatures are not

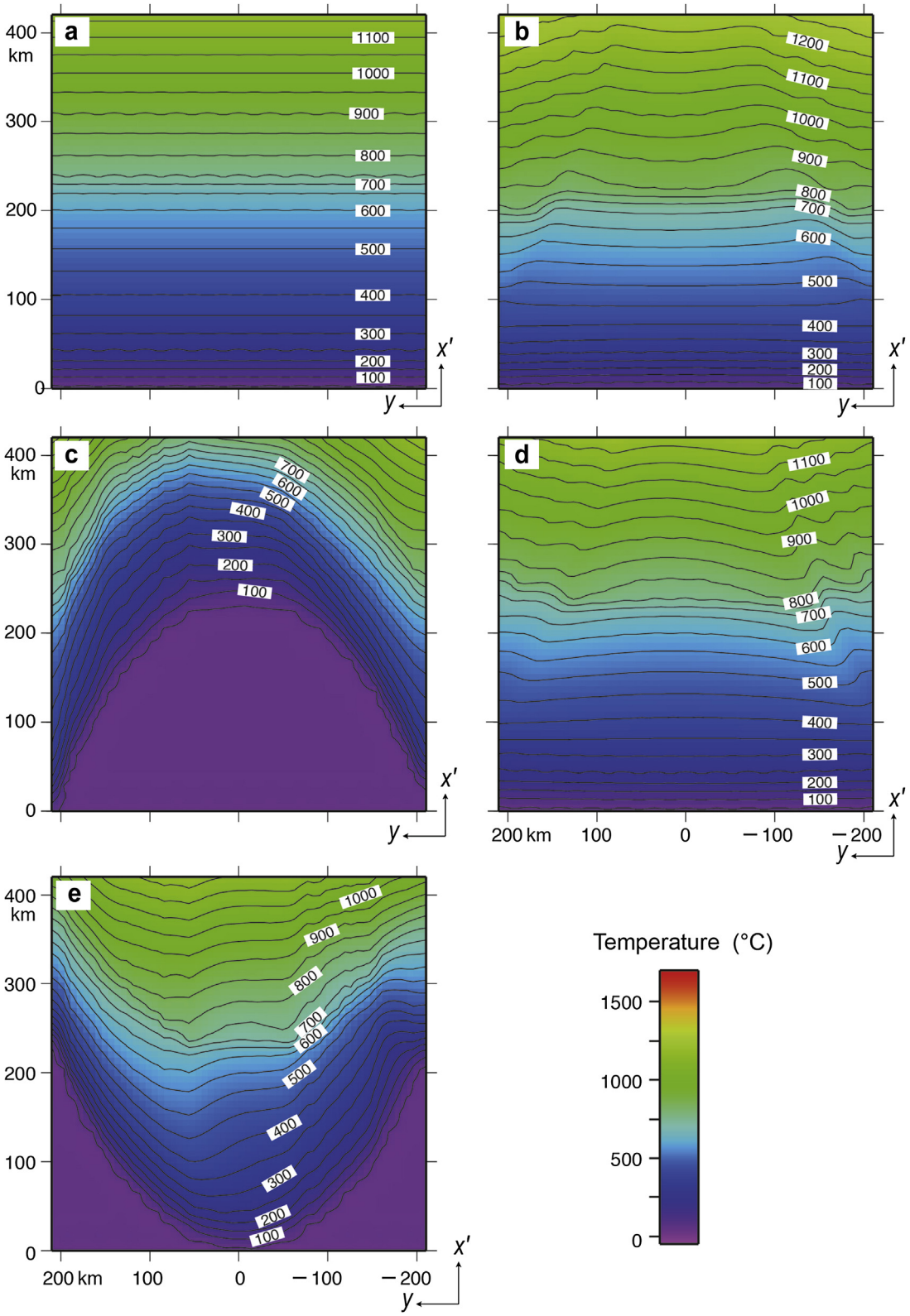

Figure 10. The interplate temperature distribution calculated for the five different slab shapes at 10 Myr. The oceanic plate subducts at 6.0 cm/yr in the direction of 30° counterclockwise from the normal direction of the trench with a dip angle of 10°. (a) Flat slab (Model 1-2). (b) Conic slab (Model 2-2). (c) Cylindrical slab (Model 3-2). (d) Inverse conic slab (Model 4-2). (e) Inverse cylindrical slab (Model 5-2).

large in Fig. 6b and d, it can be seen that the left side of Fig. 6b and right side of Fig. 6d have slightly lower temperature distributions where there are larger TSAs. To verify this trend, we checked their *y*-*z* cross-sections (Fig. 7). It is obvious that the left half of Fig. 7c and right half of Fig. 7e are cooler than the opposite sides.

In Fig. 8, it can be seen that the deeper the oceanic plate was subducted, the longer the cooling effect lasted. For example, in Fig. 8h, the effect of cooling can be identified inside the slab, whereas the same isothermal contour lines in Fig. 8g are situated in a more upward location. Therefore, it was inferred that subduction with a higher TSA generates a cooling effect on the slab surface beneath the continental plate.

The TSA is not a pure subduction angle, but a combination of the subduction angle and slab slope angle in the subduction direction. For example, for the cylindrical slab surface, the left side (Fig. 7c) had a larger slab slope angle, leading to a larger composite angle, which was critical to the cooling effect in the subduction zone associated with the subduction of an oceanic plate. For oblique subduction, we also found that the TSA was different from the nominal dip angle due to the gradient slope of the slab.

3.3. Comparison of interplate temperature

Figs. 9 and 10 show the interplate temperatures for the five models with differently shaped slabs for straight subduction and oblique subduction, respectively. In the conic and cylindrical slab models, the values of TSA were not fixed and their variation depended on the along-arc and across-arc curvatures.

The interplate temperature distribution also had a close relationship with the depth of the slab surface. For example, in Fig. 9b–e, the interplate thermal distributions have similar shapes to sections of the cone and column.

Although the slab shapes constructed in this study were symmetric, the temperature distributions were asymmetric when oblique subduction occurred (Fig. 10). Isothermal contour lines appeared to bend toward the direction of oblique subduction (Fig. 10c). Because the cooling effect by subduction depended on the different slab slope angles, the interplate temperature was also influenced by the shape of the slab. However, when the along-arc curvature varied, the different pathway of subduction led to variation in the TSA. This explains why the oblique subduction of a curved oceanic plate resulted in an asymmetric interface temperature distribution, even though the plate geometry is symmetric.

We subtracted the interplate temperature with a straight subduction (Fig. 9) from that with an oblique subduction (Fig. 10), and obtained the differences in temperatures along selected profiles for the five models (Fig. 11). The horizontal axis is the horizontal distance in the *x* direction from the trench, and the vertical axis is the difference in temperature. The three lines are the calculated results along the profiles of $y = -150$ km, $y = 0$ km, and $y = 150$ km. Fig. 11 shows that in most cases, the interplate temperature for oblique subduction was higher than that for straight subduction because the oceanic plate undergoing straight subduction was farther from the trench than the oblique one. Therefore, the cooling effect for straight subduction was more remarkable. The differently shaped slabs displayed different differences in temperature. In Fig. 11a, the differences in temperatures along the three profiles are the same, but in conic (Fig. 11b) and cylindrical (Fig. 11c) slabs, it can be seen that the differences in temperature at $y = -150$ km were larger than those at $y = 150$ km. In contrast, for the inverse conic (Fig. 11d) and inverse cylindrical shapes (Fig. 11e), the differences in temperature at $y = 150$ km were larger than those at $y = -150$ km. This implies that if the obliquity of subduction exists, its effects on interplate temperatures may be totally opposite to those that are expected. This is because the slab's along-arc curvature was directionally dependent. When the along-arc curvature along the obliquity of subduction was positive (i.e., a convex slab) or larger (such as the green curve in Fig. 11c and red curve in Fig. 11e), the interface temperature was lower. Conversely, when the along-arc curvature was negative (i.e., a concave slab) or smaller (such as the red curve in Fig. 11c and green curve in Fig. 11e), the interface temperature was higher. The oblique subduction changed the TSA due to the directionally dependent property of the plate's along-arc curvature and produced an asymmetrical interplate temperature for a symmetrically curved slab. In addition, when the surface of the slab was deep enough, the slab shape exerted a weaker effect on the variation in interplate temperature. This is because the temperature of the slab was sufficiently heated through thermal assimilation from the surrounding mantle.

3.4. Comparison of heat flow

We calculated surface heat flow, and compared the results for the differently shaped slabs (Fig. 12). Panels a–j show the results for the 10 models with five different slab shapes for straight and oblique subductions.

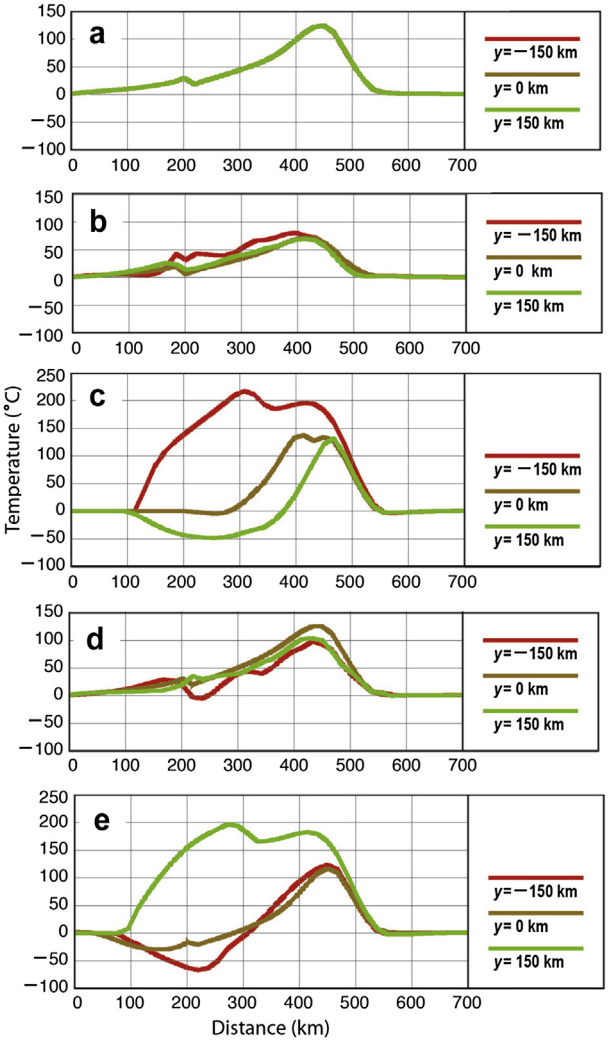

Figure 11. The interplate difference in temperature (i.e., the temperature distribution for straight subduction subtracted from the temperature distribution for oblique subduction) along three profiles ($y = -150$, 0 and 150 km) at 10 Myr. The horizontal axis is the distance from the trench in the *x* direction, and the vertical axis is the difference in temperature. (a) Flat slab (Model 1). (b) Conic slab (Model 2). (c) Cylindrical slab (Model 3). (d) Inverse conic slab (Model 4). (e) Inverse cylindrical slab (Model 5).

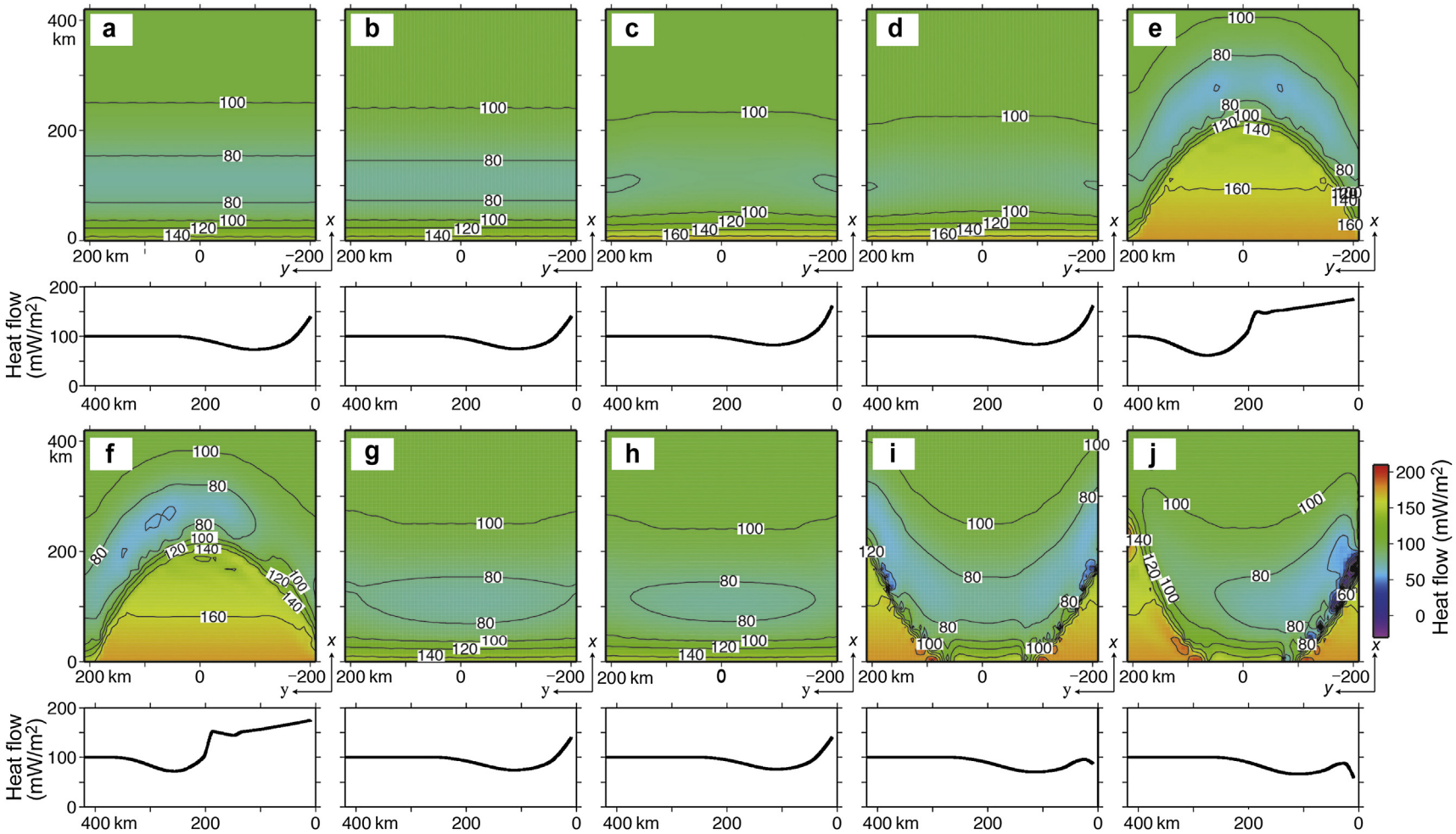

Figure 12. The surface heat flow distribution calculated at 10 Myr. The oceanic plate subducts at 6.0 cm/yr from the trench. When the oceanic plate subducts obliquely, the direction is 30° counter-clockwise from the $+x$ direction with a dip angle of 10°. The red solid line is the location of the trench. Graphs below the colored figures are the heat flow distributions along the profile $y = -105$ km. (a) Flat slab with straight subduction (Model 1-1). (b) Flat slab with oblique subduction (Model 1-2). (c) Conic slab with straight subduction (Model 2-1). (d) Conic slab with oblique subduction (Model 2-2). (e) Cylindrical slab with straight subduction (Model 3-1). (f) Cylindrical slab with oblique subduction (Model 3-2). (g) Inverse conic slab with straight subduction (Model 4-1). (h) Inverse conic slab with oblique subduction (Model 4-2). (i) Inverse cylindrical slab with straight subduction (Model 5-1). (j) Inverse cylindrical slab with oblique subduction (Model 5-2).

When the upper surface of the slab was shallower than a depth of approximately 60 km, the surface heat flow had a close relationship with the slab's geometry, which was similar to the interplate temperature distribution. However, when it was deeper than 60 km the influence on surface heat flow was negligible.

Similarly to the interplate temperature, the oblique subduction results revealed asymmetrical distributions of surface heat flow. The heat flow values on the descent slope of the slab surface were lower (Fig. 12f and j). A larger TSA was generally accompanied by a low heat flow anomaly. Comparing Fig. 10c with Fig. 12f, and Fig. 10e with Fig. 12j, which show results for the same model, we found that the influence of the TSA on heat flow was more remarkable at a shallower depth. The straight subduction of flat (Fig. 12a), conic (Fig. 12c), and inverse conic (Fig. 12g) slabs resulted in a slightly lower heat flow than oblique subduction (Fig. 12b, d and h), because the TSA was slightly larger for straight subduction than for oblique subduction.

A relationship between the TSA of the slab and surface heat flow could be identified at depths shallower than approximately 60 km. When the plate interface was deeper than 60 km, the cooling effect of the surface heat flow disappeared. Considering that the subduction angles were generally 10 to 20° at a trench, we suggest that the horizontal distance in which slab geometry is able to influence the surface heat flow could reach 300 km from the trench. Beyond this distance, the effect is likely to be negligible.

4. Discussion

The results obtained from subduction models of the curved oceanic plates showed a distinct contrast in temperature and mantle flow to those obtained for a flat slab. Along-arc mantle flow convection was more common in the subduction of an oblique curved plate. The slab radius had an influence on the radius of the convection. We also found that the TSA along the obliquity induced various differences in the temperature field. The larger the TSA, the more effective was the mantle cooling caused by subduction. The total TSA, which can be considered the average value of the TSA over the whole slab length, reflected the average subduction angle of the oceanic plate, and markedly influenced the overall temperature field and mantle flow around the slab. This can be attributed to the pattern of the temperature distribution and the surface heat flow, which had a corresponding relationship with the shape of the slab.

We found that a larger TSA also generated a cooler plate interface. In the mantle, temperature is mainly determined by depth. Hence, the interplate temperature should influence the depth of the surface of the slab and the inner slab temperature. The depth of the surface of the slab can be considered to represent the geometry of the slab, and the inner slab temperature depended on how long the slab was in contact with the hot mantle, as mentioned above, which was in turn related to the subduction pathway and true angle. Therefore, the interplate temperature distribution was related to the slab's geometry and the TSA. The influence of slab shape on interplate temperature disappeared at depths greater than 150 km because the cool slab became as hot as the surrounding upper mantle. In addition, for oblique subduction, the rate of change in the TSA depended on both the along-arc and across-arc plate curvature. Therefore, a larger along-arc plate curvature could cause greater variation in the TSA and furthermore could cause greater variation in the interplate temperature. Based on many calculations, the rate of temperature change for the TSA was about 0.05–0.25 °C/(°km) ($10^\circ < \mathrm{TSA} < 20^\circ$) for an increased unit length of the slab at the depth range $[\overline{TSA} \times 5 - 50\ \mathrm{km}, \overline{TSA} \times 5 + 10\ \mathrm{km}]$ (where $\overline{TSA}$ is the average TSA for the whole subduction process, and $10^\circ < \overline{TSA} < 20^\circ$).

Previous studies have seldom referred to the along-arc plate curvature, and discussions of arc curvature are mostly used to interpret the arc roll-back and advance. Yoshioka and Murakami (2007) studied the thermal regime in the plate interface beneath southwest Japan, and reported that distribution of temperature at the plate interface was similar to the slab geometry. However, the relationship between the along-arc heterogeneity of interplate temperature and slab curvature has not been considered. Therefore, this study is unique in presenting data on how along-arc plate curvature influences the plate interface temperature due to a changing TSA.

Finally, the distribution of surface heat flow also corresponded to the slab geometry, which was related to the value of the TSA. A steeply subducting oceanic plate resulted in a lower surface heat flow than a gently subducting plate because of the existence of a cooler plate interface at a depth shallower than 60 km, which was due to the larger TSA. A low heat flow anomaly appeared on the descent slope of the slab surface, which can also be interpreted as being a consequence of a larger TSA. Similarly the effect of the along-arc curvature explained why the oblique subduction led to asymmetry of the surface heat flow distribution, even when the shape of the slab was symmetric. The sensitive zone where TSA had an influence on the surface heat flow was in the depth range of 0 to 50 km, and the rate of change in the heat flow was $\sim 3\ \mathrm{mW/(m^2\,^\circ)}$ when $\mathrm{TSA} > 5^\circ$.

5. Conclusions

We constructed 3D thermal convection models of five curved slabs with flat, conic, cylindrical, inverse conic, and inverse cylindrical shapes. After 10 Myrs of subduction, the distribution of temperature, mantle flow, and heat flow differed due to the different slab shapes. By investigating these differences, significant conclusions can be obtained as follows:

(1) The mantle cooling caused by subduction of the oceanic plate is affected by the TSA of a slab, which is a combination of the dip angle and subduction obliquity. A slab with a larger TSA will have a larger mantle cooling effect and a lower interplate temperature. The rate of temperature change for the TSA of the interplate is 10–50 °C/° ($10^\circ < \mathrm{TSA} < 20^\circ$), within the depth range of $\mathrm{TSA} \times 5 - 50$ km to $\mathrm{TSA} \times 5 + 10$ km for a flat slab after subduction of 7 Myrs.

(2) Oblique subduction has a remarkable effect on temperature and mantle flow. Even a symmetric slab shape can have asymmetric patterns of temperature and mantle flow under oblique subduction. This is because the slab's TSA is changed by oblique subduction and the along-arc curvature contributes to the variation in the TSA, which changes the interplate thermal regime. The rate of change in the TSA depends on the slab curvature along the subduction pathway. The effects of obliquity and slab geometry on interplate temperature were clarified by our various subduction models with an arbitrary shape for the oceanic plate.

(3) The shape of the slab surface has a corresponding relationship with the distribution of surface heat flow. The pattern of surface heat flow is very similar to the slab geometry. The most sensitive zone for the surface heat flow to be influenced by the TSA is at depths of less than 50 km, with a change in the rate of heat flow of $\sim 3\ \mathrm{mW/(m^2\,^\circ)}$ when $TSA > 5^\circ$. If the slab surface is deeper than 60 km, its influence on surface heat flow disappears due to the increased depth.

Acknowledgments

We thank P. J. Tackley for sharing the original 3D source codes for our numerical simulation. We also thank T. Gerya, M. Yoshida

and an anonymous reviewer for their constructive comments. Some figures were created using the Generic Mapping Tools developed by Wessel and Smith (1998).

Appendix

The parameters and properties of the constructed slab model described here include initialization of the slab curvature, slab geometry (depth of plate interface), and prescribed subduction velocity.

1. Slab curvature

Curvature, as a function of the distance from the trench axis is defined as follows:

$$C(x,y) = \alpha(y)\beta(x) \tag{A1}$$

with

$$\alpha(y) = \frac{4my_{\max}z_{\max}}{\left\{(2z_{\max}^2 - y_{\max}^2)\left(\frac{2y}{y_{\max}}+1\right)^2 + y_{\max}^2\right\}^{\frac{3}{2}}} \tag{A2}$$

$$\beta(x) = \exp\left[\frac{(x-x_1)\{\log C(x_{\max}) - \log C(x_1)\}}{x_{\max}-x_1}\right] + C(x_1) \quad x \geq x_1 \tag{A3}$$

$$\beta(x) = \exp\left[\frac{(x-x_0)\{\log C(x_1) - \log C(x_0)\}}{x_1-x_0}\right] + C(x_0) \quad x_0 \leq x \leq x_1, \tag{A4}$$

where x, y, and z are the distance from the trench axis, distance from the right-middle profile, and depth from the model surface, respectively. $x_{\max}$, $y_{\max}$, and $z_{\max}$ are the side lengths of the model box ($x_{\max}$ = 771 km, $y_{\max}$ = 420 km, and $z_{\max}$ = 300 km). The domain of variables is $0 \leq x \leq 771$ (km), $-210 \leq y \leq 210$ (km), and $0 \leq z \leq 300$ (km). $C(x,y)$ is the curvature at grid (x,y), which is x km from the trench axis and y km from the middle profile. x_0 and x_1 are assumed to be 0 and 64, respectively. $C(x_0)$, $C(x_1)$, and $C(x_{\max})$ are amplification factors on the middle axis ($y = 0$) of distances x_0, x_1, and $x_{\max}$, respectively, and they are given as constants, which allow the shape of a slab to be designated. $\alpha(y)$ is the curvature formula of variable y in an ellipse with the major axis radius $a = y_{\max}/2$ and minor axis radius $b = z_{\max}$. $m = \pm 1$ indicates either a positive or negative curvature. $\beta(x)$ is the amplification factor of the ellipse curve at a distance of x.

2. Slab geometry

The depth of the slab surface at point (x, y) is defined as

$$Z(x,y) = \frac{z_{\max}}{x_{\max}}x + m\beta(x)z_{\max}\left\{1 - \sqrt{1-\left(\frac{2y}{y_{\max}}\right)^2}\right\} \tag{A5}$$

The curvature and depth at point (x, y) are designated by these formulae so that slab shape is fixed and prescribed in the numerical simulation.

The modeling space was divided into four parts (Fig. 1a and b), namely, the upper crust, lower crust, slab, and mantle. The thickness of both the upper and lower crusts was assumed to be 16 km. We assumed that the continental crust is rigid and that the thermal conductivity of the crust is 2.5 W/(m °C). The length of a slab increased with time spent at a given subduction velocity. When subduction of the oceanic plate occurs, the slab extends into the modeling space, and the subsequent dynamic mantle flow can be calculated. If the value of m is assumed to be -1, the shape of a slab is reversed by 180°. Table 2 gives the values of the model parameters used for models 1-1 to 5-2. All of the oceanic plates were subducted for 10 Myr, and the subduction velocity was determined as 6.0 cm/yr for straight forward or 30° from $+x$ counter-clockwise for oblique subduction. Because all of the slab models were symmetric against the x axis, the thermal state and flow patterns were expected to be symmetric when the subduction of the oceanic plate was normal to the trench axis.

Table 2
The values of model parameters for definition of slab shape function in the modeling.

Model type	Model	1/C (x_0)	1/C (x_1)	1/C ($x_{\max}$)	m (plus-minus)
Flat	1-1, 1-2	0	0	0	+1
Conic	2-1, 2-2	10	0.1	0	+1
Cylindrical	3-1, 3-2	1.67	1.67	1.67	+1
Inverse conic	4-1, 4-2	10	0.1	0	−1
Inverse cylindrical	5-1, 5-2	1.67	1.67	1.67	−1

3. Prescribed subduction velocity

Although the velocity at each point inside the slab is given as a constant of 6.0 cm/yr, its components depend on the gradient slope of the slab surface. A larger vertical velocity component exists within a steeper slab. By setting this, we can guarantee that the oceanic plate always subducts inside its prescribed shape with a constant subduction velocity. Grid points inside the slab always have a velocity given as:

$$v_x(x,y,z) = \frac{-2a(x,y)b(x,y)v_y + \sqrt{\{2a(x,y)b(x,y)v_y\}^2 - 4\left\{a(x,y)^2+1\right\}\left[\left\{a(x,y)^2+1\right\}v_y^2 - v^2\right]}}{2\left\{a(x,y)^2+1\right\}} \tag{A6}$$

$$v_y(x,y,z) = v_y \tag{A7}$$

$$v_z(x,y,z) = a(x,y)v_x + b(x,y)v_y \tag{A8}$$

with:

$$a(x,y) = \frac{1}{2}\{Z(x+\xi,y) - Z(x-\xi,y)\}\cdot\frac{z_{\max}}{x_{\max}} \tag{A9}$$

$$b(x,y) = \frac{1}{2}\{Z(x+\xi,y+\zeta) - Z(x+\xi,y) + Z(x-\xi,y) - Z(x-\xi,y-\zeta)\}\cdot\frac{z_{max}}{y_{max}} \quad \text{(A10)}$$

where $v_x(x, y, z)$ and $v_z(x, y, z)$ are velocity components associated with subduction of the oceanic plate in the $+x$ and $+z$ directions, respectively; $v_y = 6.0 \times \sin30°$; $Z(x + \xi, y + \zeta)$ is the depth at grid $(x + \xi, y + \zeta)$, and so on. ξ and ζ are the smallest intervals between two neighboring grids along the x and y axes, respectively. z_{max} and y_{max} are the length and a half width of the model box along the z and y axes, respectively.

References

Bengtson, A.K., van Keken, P.E., 2012. Three-dimensional thermal structure of subduction zones: effects of obliquity and curvature. Solid Earth Discussions 4, 919–941.

Bonnardot, M.A., Hassani, R., Tric, E., Ruellan, E., Regnier, M., 2008. Effect of margin curvature on plate deformation in a 3D numerical model of subduction zones. Geophysical Journal International 173, 1084–1094.

Buffett, B.A., 2006. Plate bending at subduction zones. Journal of Geophysical Research 111, B09405. http://dx.doi.org/10.1029/2006JB004295.

Capitanio, F.A., Morra, G., 2012. The bending mechanics in a dynamic subduction system: constraints from numerical modelling and global compilation analysis. Tectonophysics 522–523, 224–234.

Capitanio, F.A., Morra, G., Goes, S., 2009. Dynamics of plate bending at the trench and slab-plate coupling. Geochemistry, Geophysics, Geosystems 10, Q04002. http://dx.doi.org/10.1029/2008GC002348.

Chemenda, A., Lallemand, S., Bokun, A., 2000. Strain partitioning and interplate friction in oblique subduction zones: constraints provided by experimental modeling. Journal of Geophysical Research 105 (B3), 5567–5581.

Christensen, U.R., 1996. The influence of trench migration on slab penetration into the lower mantle. Earth and Planetary Science Letters 140, 27–39.

Conrad, C.P., Hager, B.H., 1999. Effects of plate bending and fault strength at subduction zones on plate dynamics. Journal of Geophysical Research 104 (B8), 17551–17571.

Doin, M.P., Henry, P., 2001. Subduction initiation and continental crust recycling: the roles of rheology and eclogitization. Tectonophysics 342, 163–191.

Fukao, Y., Widiyantoro, S., Obayashi, M., 2001. Stagnant slabs in the upper and lower mantle transition region. Reviews of Geophysics 39 (3), 291–323. http://dx.doi.org/10.1029/1999RG000068.

Gerya, T., 2011. Future directions in subduction modeling. Journal of Geodynamics 5, 344–378.

Giuseppe, E.D., van Hunen, J., Funiciello, F., Faccenna, C., Giardini, D., 2008. Slab stiffness control of trench motion: insights from numerical models. Geochemistry, Geophysics, Geosystems 9, Q02014. http://dx.doi.org/10.1029/2007GC001776.

Gurnis, M., Hall, C., Lavier, L., 2004. Evolving force balance during incipient subduction. Geochemistry, Geophysics, Geosystems 5, Q07001.

Hirose, F., Nakajima, J., Hasegawa, A., 2008. Three-dimensional seismic velocity structure and configuration of the Philippine Sea slab in southwestern Japan estimated by double-difference tomography. Journal of Geophysical Research 113, B09315.

Honda, S., 1997. Mantle Dynamics II—Mechanics, in Iwanami-koza Earth and Planetary Science 10 Dynamics of the Earth's Interior. Iwanami-Shoten, Tokyo, pp. 73–121 (in Japanese).

Honda, S., 2009. Numerical simulations of mantle flow around slab edges. Earth and Planetary Science Letters 277, 112–122.

Honda, S., Gerya, T., Zhu, G., 2010. A simple three-dimensional model of thermochemical convection in the mantle wedge. Earth and Planetary Science Letters 290, 311–318.

Honda, S., Saito, M., 2003. Small-scale convection under the back-arc occurring in the low viscosity wedge. Earth and Planetary Science Letters 216, 703–715.

Honda, S., Yoshida, T., 2005. Application of the model of small-scale convection under the island arc to the NE Honshu subduction zone. Geochemistry, Geophysics, Geosystems 6, Q01002.

Honda, S., Yoshida, T., Aoike, K., 2007. Spatial and temporal evolution of arc volcanism in the northeast Honshu and Izu-Bonin arcs: evidence of small-scale convection under the island arc? Island Arc 16, 214–223.

Iwamori, H., 1997. Heat sources and melting in subduction zones. Journal of Geophysical Research 102, 14803–14820.

Jadamec, M.A., Billen, M.I., 2010. Reconciling surface plate motions with rapid three-dimensional mantle flow around a slab edge. Nature 465, 338–341.

Morra, G., Regenauer-Lieb, K., Giardini, D., 2006. Curvature of oceanic arcs. Geology 34, 877–880.

Morra, G., Yuen, D.A., Boschi, L., Chatelaine, P., Koumoutsakose, P., Tackley, P.J., 2010. The fate of the slabs interacting with a density/viscosity hill in the mid-mantle. Physics of the Earth and Planetary Interiors 180, 271–282.

Nakajima, J., Hasegawa, A., 2007. Subduction of the Philippine Sea plate beneath southwestern Japan: slab geometry and its relationship to arc magmatism. Journal of Geophysical Research 112, B08306.

Ribe, N.M., 2010. Bending mechanics and mode selection in free subduction: a thin-sheet analysis. Geophysical Journal International 180, 559–576. http://dx.doi.org/10.1111/j.1365-246X.2009.04460.x.

Schellart, W.P., Freeman, J., Stegman, D.R., Mores, L., May, D., 2007. Evolution and diversity of subduction zones controlled by slab width. Nature 446, 308–311.

Stadler, G., Gurnis, M., Burstedde, C., Wilcox, L.C., Alisic, L., Ghattas, O., 2010. The dynamics of plate tectonics and mantle flow: from local to global scales. Science 329, 1033–1038.

Stegman, D.R., Freeman, J., Schellart, W.P., Moresi, L., May, D., 2006. Influence of trench width on subduction hinge retreat rates in3D models of slab rollback. Geochemistry, Geophysics, Geosystems 7, Q03012.

Tackley, P.J., 1998. Self-consistent generation of tectonic plates in three-dimensional mantle convection. Earth and Planetary Science Letter 157, 9–22.

Tackley, P.J., 2000. Self-consistent generation of tectonic plates in time-dependent, three-dimensional mantle convection simulations 2. Strain weakening and asthenosphere. Geochemistry Geophysics Geosystems 1, 1026. http://dx.doi.org/10.1029/2000GC000043.

Tackley, P.J., Xie, S., 2003. Stag3D: a code for modeling thermo-chemical multiphase convection in Earth's mantle. Proceedings of the Second MIT Conference on Computational Fluid and Solid Mechanics.

Torii, Y., Yoshioka, S., 2007. Physical conditions producing slab stagnation: constraints of the Clapeyron slope, mantle viscosity, trench retreat, and dip angles. Tectonophysics 445 (3–4), 200–209.

Toth, J., Gurnis, M., 1998. Dynamics of subduction initiation at pre-existing fault zones. Journal of Geophysical Research 103, 18053–18067.

van Keken, P.E., Ballentine, C.J., 1991. Dynamical models of mantle volatile evolution and the role of phase transitions and temperature-dependent rheology. Journal of Geophysical Research 104, 7137–7151.

van Keken, P.E., Currie, C., King, S.D., Behn, M.D., Cagnioncle, A., He, J., Katz, R.F., Lin, S.C., Parmentier, E.M., Spiegelman, M., Wang, K., 2008. A community benchmark for subduction zone modeling. Physics of the Earth and Planetary Interiors 171, 187–197.

Wang, K., Hyndman, R.D., Yamano, M., 1995. Thermal regime of the Southwest Japan subduction zone: effects of age history of the subducting plate. Tectonophysics 248, 53–69.

Wessel, P., Smith, W.H.F., 1998. New, improved version of the generic mapping tools released. EOS Transactions American Geophysical Union 79, 579.

Yoshii, T., 1975. Regionality of group velocities of Rayleigh waves in the Pacific and thickening of the plate. Earth and Planetary Science Letters 25, 305–312.

Yoshida, M., Tajima, F., Honda, S., Morishige, M., 2012. The 3D numerical modeling of subduction dynamics: plate stagnation and segmentation, and crustal advection in the wet mantle transition zone. Journal of Geophysical Research 117, B04104.

Yoshioka, S., Murakami, K., 2007. Temperature distribution of the upper surface of the subducted Philippine Sea plate, southwest Japan, from a three-dimensional subduction model: relation to large interplate and low-frequency earthquakes. Geophysical Journal International 171, 302–315.

Zhao, D., Yanada, T., Hasegawa, A., Umino, N., Wei, W., 2012. Imaging the subducting slabs and mantle upwelling under the Japan Islands. Geophysical Journal International 190, 816–828.

Zhu, G., Gerya, T.V., Yuen, D.A., Honda, S., Yoshida, T., Connolly, J.A.D., 2009. 3D dynamics of hydrous thermal-chemical plumes in oceanic subduction zones. Geochemistry, Geophysics, Geosystems 10, Q11006.

Zhu, G., Gerya, T.V., Honda, S., Tackley, P.J., Yuen, D.A., 2011. Influences of the buoyancy of partially molten rock on3D plume patterns and melt productivity above retreating slabs. Physics of the Earth and Planetary Interiors 185, 112–121.